

1
2 **A global map of RNA binding protein occupancy guides functional dissection**
3 **of post-transcriptional regulation of the T cell transcriptome**

4 **Authors:** Adam J. Litterman¹, Wandi S. Zhu¹, Robin Kageyama¹, Wenxue Zhao^{2,3}, Noah
5 Zaitlen², David J. Erle², K. Mark Ansel^{1*}

6 **Affiliations:**

7 ¹ Department of Microbiology & Immunology and Sandler Asthma Basic Research Center
8 University of California San Francisco, San Francisco, CA

9 ² Department of Medicine and Lung Biology Center, University of California San Francisco, San
10 Francisco, CA

11 ³ School of Basic Medicine (Shenzhen), Sun Yat-Sen University, Guangzhou 510080, People's
12 Republic of China

13

14 *For correspondence: Mark.Ansel@ucsf.edu

15

16 **Abstract:** RNA binding proteins (RBPs) mediate constitutive RNA metabolism and gene
17 specific regulatory interactions. To identify RNA cis-regulatory elements, we developed
18 GCLiPP, a biochemical technique for detecting RBP occupancy transcriptome-wide. GCLiPP
19 sequence tags corresponded with known RBP binding sites, specifically correlating to abundant
20 cytosolic RBPs. To demonstrate the utility of our occupancy profiles, we performed functional
21 dissection of 3' UTRs with CRISPR/Cas9 genome editing. Two RBP occupied sites in the CD69
22 3' UTR destabilized the transcript of this key regulator of lymphocyte tissue egress. Comparing
23 human Jurkat T cells and mouse primary T cells uncovered hundreds of biochemically shared
24 peaks of GCLiPP signal across homologous regions of human and mouse 3' UTRs, including a
25 cis-regulatory element that governs the stability of the mRNA that encodes the proto-oncogene
26 PIM3 in both species. Our GCLiPP datasets provide a rich resource for investigation of post-
27 transcriptional regulation in the immune system.

28

29 **Introduction**

30 The life cycle of protein coding RNA transcripts involves their transcription from DNA,
31 5' capping, splicing, 3' polyadenylation, nuclear export, targeting to the correct cellular
32 compartment, translation and degradation (Beelman and Parker, 1995; Martin and Ephrussi,
33 2009; Reed, 2003). RNA binding proteins (RBPs) coordinately regulate these processes through
34 interaction with RNA cis-regulatory elements, often in the 5' and 3' untranslated regions (UTRs)

35 whose sequences are not constrained by a functional coding sequence (Keene, 2007).
36 Mammalian genomes encode hundreds of RBPs (Castello et al., 2012), and mutations in
37 individual RBPs or even individual binding sites can induce strong developmental, autoimmune
38 and neurological defects in human patients and mouse models (Bassell and Kelic, 2004; Kafasla
39 et al., 2014; Schwerk and Savan, 2015). As much as half of the extensive gene expression
40 changes that occur during T cell activation occur post-transcriptionally (Raghavan et al., 2002),
41 and several RBPs are known to be critical determinants of immune function and homeostasis
42 (Kafasla et al., 2014).

43 Methods like DNase I hypersensitivity and ATAC-seq that query regulatory element
44 accessibility and occupancy without prior knowledge of their protein binding partners have
45 proven themselves as powerful techniques for the systematic mapping of *cis*-regulatory
46 sequences in DNA (Buenrostro et al., 2013; Thurman et al., 2012). Their development has
47 allowed for comparisons in the regulatory structure of diverse cell types (Corces et al., 2016) and
48 across the tree of life (Villar et al., 2015; Wilson et al., 2008). A lack of analogous systematic
49 methods for mapping the transcriptome's *cis*-regulatory landscape has limited our understanding
50 of post-transcriptional regulatory circuits and the evolution of untranslated regions of transcribed
51 genes.

52 Current methods for regulatory element identification in RNA have focused on specific
53 *trans* factors (Lee and Ule, 2018), although more recent technologies have also analyzed
54 secondary structure (Spitale et al., 2015) and interaction with chromatin (Li et al., 2017)
55 transcriptome wide. Protein precipitation (Baltz et al., 2012) and chemical biotinylation of
56 proteins (Freeberg et al., 2013) have been used to analyze global RBP occupancy in cell lines
57 and yeast, respectively, but difficulty remains in defining RNA regulatory activity in a

58 systematic way. Here, we create global RBP occupancy maps for a human T cell line, Jurkat, and
59 primary mouse T cells. Comparing RBP occupancy for thousands of mRNAs across species
60 identified biochemically shared regulatory sites, which are enriched for phylogenetically
61 conserved sequences. Finally, we used a scalable system of CRISPR dissection to define regions
62 of functional activity in 3' UTRs of mouse and human transcripts of immunological importance.
63 Biochemically derived maps of RBP occupancy are a powerful tool for the interrogation of post-
64 transcriptional gene regulation in the immune system.

65

66 **Results**

67 Transcriptome-wide analysis of RBP occupancy in T cells in two species

68 To achieve transcriptome-wide RBP binding site profiling, we developed a protocol for
69 Global Cross-linking Protein Purification (GCLiPP) suitable for use in mammalian cells and
70 applied this technique in human Jurkat T cells and cultured primary mouse T cells (Figure 1A).
71 GCLiPP is an adaptation of previously described biochemical methods for crosslinking
72 purification of all mRNA-RBP complexes. The key features of GCLiPP include: crosslinking of
73 endogenous ribonucleoprotein complexes using high energy UV light (no photo-crosslinkable
74 ribonucleotide analogues); oligo-dT pulldown prior to biotinylation to enrich for mRNA species;
75 chemical biotinylation of primary amines using a water soluble reagent with a long, flexible
76 linker; brief RNase digestion with RNase T1; and on-bead linker ligation with radiolabeled 3'
77 linker to facilitate downstream detection of ligated products. We used the guanine specific
78 ribonuclease T1 to favor larger average fragment sizes than using an RNA endonuclease with no
79 nucleotide specificity (such as RNase A) and ligated RBP protected fragments into a small RNA
80 sequencing library.

81 We called local peaks of GCLiPP sequence read density and measured the distribution of
82 GCLiPP reads within those peaks to assess the reproducibility of the technique. Local read
83 density within individual transcripts was similar between experiments, as GCLiPP fragments
84 yielded highly reproducible patterns in technical replicates (e.g. comparing replicate Jurkat T cell
85 samples, Figure 1B) and across multiple pooled experiments (e.g. comparing CD4⁺ and CD8⁺ T
86 cells, Figure 1C). A similar distribution of transcriptome features constituted GCLiPP libraries
87 from both Jurkat and primary T cells, with read coverage strongly enriched within mature
88 mRNAs and long non-coding RNAs (Figure 1D,E). The most striking difference was the greater
89 proportion of reads derived from transposable elements in mouse GCLiPP libraries. This
90 increase is likely due to the greater amount of annotated transposable elements in the mouse
91 genome since the relative coverage of these elements was similar between species.

92

93 GCLiPP read density represents cytosolic RBP occupancy

94 To validate GCLiPP, we systematically examined the relationship between GCLiPP
95 occupancy profiles in human Jurkat cells and enhanced cross-linking immunoprecipitation
96 (eCLIP) analyses of specific RBP binding profiles in K562 cells from the Encyclopedia of DNA
97 Regulatory Elements (ENCODE) project (Sundararaman et al., 2016). We examined pairwise
98 correlations of normalized read density across individual 3' UTRs between GCLiPP and
99 individual RBP eCLIP samples to identify contributions of each RBP, and also compared
100 GCLiPP and the input control for each eCLIP experiment (Figure 2A). eCLIP for many RBPs,
101 such as TIA1 and IGF2BP1, more closely matched GCLiPP read density than the eCLIP control
102 input across the genome (Figure 2B). We also found RBPs, such as PUM2, that exhibited anti-
103 correlations with GCLiPP signal across individual transcripts. In these cases, we typically saw

104 focal RBP binding to specific sites within transcripts (such as UGUA motifs in the case of
105 PUM2) that, while represented in GCLiPP reads, did not dominate the GCLiPP signal (Figure
106 2A, bottom panel). Although the PUM2 eCLIP profile did not correlate to GCLiPP signal
107 genome wide, PUM2 binding sites were still overrepresented in GCLiPP data. This was revealed
108 when we called GCLiPP peaks with CLIPper (Lovci et al., 2013) and compared these peaks with
109 CLIPper called peaks in eCLIP datasets. The observed fraction of PUM2 eCLIP peaks that
110 overlap GCLiPP peaks (0.56) was much greater than the fraction overlapping eCLIP peaks
111 randomly shuffled across the 3' UTRs from which they were derived (Figure 2C, bottom panel).
112 Similar results were obtained for TIA-1 (Figure 2C, top panel) and IGF2BP1 (Figure 2C, middle
113 panel). These enrichments above background binding for IGF2BP1, TIA1 and PUM2 were
114 amongst the highest 8 of the 87 RBPs whose eCLIP signals were examined (Supplementary
115 Figure 1).

116 We performed genome wide correlation analysis for 87 RBPs obtained from eCLIP data,
117 and compared the correlation between eCLIP and GCLiPP with RBP abundance previously
118 determined via mass spectrometry (Baltz et al., 2012). There was an overall significant
119 correlation between RBP abundance and correspondence between RBP eCLIP and GCLiPP
120 profiles ($r=0.28$, $p=.022$). However, stratifying RBPs by their predominant cellular localization
121 (Binder et al., 2014) showed that this correlation was driven almost entirely by cytosolic RBPs
122 (Figure 2D). The fraction of eCLIP peaks that overlapped GCLiPP peaks above a shuffled
123 background was also significantly greater for cytosolic versus non-cytosolic RBPs ($p=0.003$,
124 Supplementary Figure 1 inset). These findings were expected, as the GCLiPP experimental
125 protocol preferentially samples the cytosol by eliminating most nuclear material. In summary, we
126 conclude that GCLiPP read density reflects transcriptome-wide cytosolic RBP occupancy.

127

128 RBP Occupancy of known RNA cis-regulatory elements in primary T cells

129 We examined the GCLiPP profiles at previously characterized cis-regulatory elements of
130 various functional and structural categories in primary mouse T cells. The canonical
131 polyadenylation signal AAUAAA is a known linear sequence motif that binds to a number of
132 RBPs in the polyadenylation complex, including CPSF and PABP (Millevoi and Vagner, 2009),
133 as part of constitutive mRNA metabolism. We examined T cell lineage-defining transcripts with
134 well-resolved GCLiPP profiles (due to their high expression levels), including *Cd3g* (Figure 3A),
135 *Cd3e*, *Cd4*, and *Cd8b1* (Supplementary Figure 2). The only canonical polyadenylation signal
136 sequences in these transcripts were contained within called GCLiPP peaks, often as the peak
137 with the highest GCLiPP read density in the entire transcript. Interestingly, the GCLiPP profile
138 of *Cd8b1* contained direct biochemical evidence for alternative polyadenylation signal usage
139 (Figure S2C), a phenomenon that has previously been described to be important in activated T
140 cells (Sandberg et al., 2008). GCLiPP peaks appeared in multiple canonical polyadenylation
141 signal sequences in *Cd8b1*, coincident with clear evidence for both short and long 3' UTR
142 isoform usage indicated by lower RNAseq read counts after the initial canonical polyadenylation
143 signal. A similar pattern was also apparent in *Hif1a* (Figure S1D) and a number of other highly
144 expressed transcripts.

145 Known cis-regulatory elements involved in transcript localization were also represented
146 by local regions of GCLiPP read density. The Beta-actin “zipcode” element is responsible for
147 localization of *Actb* mRNA to the cellular leading edge in chicken embryo fibroblasts (Kislauskis
148 et al., 1994) and contains conserved linear sequence elements separated by a variable linker.
149 These conserved sequence elements are thought to form the RNA/protein contacts in a complex

150 involving the actin mRNA and the RNA binding protein Igf2bp1 (previously known as Zbp1)
151 where the non-conserved sequence winds around the RBP (Chao et al., 2010). This sequence
152 corresponds to the center of the second highest peak of GCLiPP read density in the *Actb*
153 transcript (Figure 3B). Some RBPs regulate the half-life and/or translation of the mRNAs that
154 they bind. The mRNA-destabilizing Roquin/Regnase binding site in the 3' UTR of *Ier3* is a
155 straightforward example of this functional category of RNA/RBP interaction detected as a region
156 of GCLiPP read density (Figure 3C).

157 The insertion of the selenium containing amino acid selenocysteine into selenoproteins
158 represents a unique case of RBP regulation of protein translation. Selenoproteins are redox
159 enzymes that use selenocysteine at key reactive residues (Johansson et al., 2005; Papp et al.,
160 2007) Selenocysteine is encoded by the stop codon UGA, and this recoding occurs only in
161 mRNAs that contain 3' UTR *cis*-regulatory elements (termed SECIS elements) that bind to RBPs
162 that recruit the elongation factor Eefsec and selenocysteine-tRNA (Berry et al., 1993; Tujebajeva
163 et al., 2000). SECIS elements were prominent peaks of GCLiPP read coverage in selenoprotein
164 mRNAs. For example, the predicted SECIS element (Mariotti et al., 2013) in the 3' UTR of *Gpx4*
165 was entirely covered by GCLiPP reads (Figure 3D). Indeed, a canonical polyadenylation signal
166 and the full hairpin structure containing the SECIS element account for essentially all of the
167 GCLiPP reads in the *Gpx4* 3' UTR (Figure 3E). Comparing transcriptome-wide in vivo folding
168 data from icSHAPE (Spitale et al., 2015) and GCLiPP data supports the identification of an RBP
169 bound, structured SECIS element (Figure 3F,G). Furthermore, this analysis suggests that the
170 folded, RBP bound structure is even larger than that predicted by SECISearch 3, with regions of
171 GCLiPP read density and apposed high and low icSHAPE signals spanning almost the entire 3'
172 UTR. Thus, GCLiPP recapitulated previously described *cis*-regulatory elements that mediate

173 constitutive RNA metabolism, transcript localization, regulation of gene expression, and
174 translation, including both structured elements and single-stranded RNA determinants.

175

176 GCLiPP-guided CRISPR dissection of immune gene post-transcriptional regulation

177 We then sought to use our GCLiPP RBP occupancy profiles to guide experimental
178 dissection of the post-transcriptional regulation of immunologically important transcripts. We
179 first focused on CD69, a cell surface C-type lectin protein transiently upregulated on T cells
180 early during activation. CD69 inhibits lymphocyte egress from lymphoid organs, and has been
181 implicated in a variety of other immune cell functions (Cibrián and Sánchez-Madrid, 2017). As
182 *CD69* mRNA is a labile transcript (Santis et al., 1995) we sought to identify cis-regulatory
183 elements in the 3'UTR that regulate stability. First, we designed guide RNAs (gRNA) targeting
184 nucleotide positions 57 and 784 downstream of the stop codon to generate large deletions in the
185 3'UTR by transfecting CRISPR-Cas9 ribonucleoprotein complex (crRNP) in Jurkat cells. From
186 the pool of transfected cells, we generated a clone (3'UTR Δ 57-784) that contained two mutant
187 alleles with deletions that spanned positions 22 to 853 and 44 to 833 of *CD69* 3' UTR (Figure
188 4A). As a control, we generated a wildtype (WT) clone from Jurkat cells transfected with a
189 scrambled control gRNA crRNP. Homozygous deletion of most of the *CD69* 3' UTR led to
190 higher basal expression of CD69 protein (Figure 4B, left) and higher expression after stimulation
191 with PMA and Ionomycin (Figure 4B, right). Importantly, the *CD69* transcript in the 3'UTR
192 Δ 57-784 clone decayed at a much slower rate, with a half-life of greater than 3 hours compared
193 to 0.36 hours in WT Jurkat cells after global transcriptional inhibition with actinomycin D
194 (Figure 4C). This effect was specific to *CD69* as the half-life of dual-specific phosphatase 2
195 (*DUSP2*), another labile transcript, was similar in WT and mutant clones (Figure 4C). These data

196 indicate that the *CD69* 3'UTR contains destabilizing cis-regulatory elements responsible for the
197 short half-life of the mRNA.

198 To determine whether RBP-occupied sites in the 3'UTR contain cis-regulatory elements
199 that regulate stability, we performed CRISPR-Cas9 dissection of the region (Zhao et al., 2017).
200 Using the GCLiPP profile as a guide, we designed 6 gRNAs along the 3'UTR, transfected them
201 as a crRNP pool into Jurkat cells, and (RT)-PCR amplified the *CD69* 3' UTR from genomic
202 DNA and RNA from transfected cells (Figure 4D). The dissection led to many distinct short and
203 long deletions (Figure 4E) that possessed destabilizing activity, indicated by a high RNA/gDNA
204 ratio relative to the predicted WT allele as measured by microcapillary gel electrophoresis
205 (Figure 4F). To determine whether certain RBP-occupied regions had greater destabilizing
206 activity than others, we sequenced amplicon fragments to measure the relative abundance of
207 transcripts containing the various deletions (Figure 4— source data 1), analyzed deletions
208 <250bp and calculated relative RNA/gDNA ratios along the 3'UTR. Our analysis revealed
209 varying deletion sizes (Figure 4G) and identified two regions with the highest destabilizing
210 activity that correspond with GCLiPP peaks (protein occupied regions PR1 and PR2 in Figure
211 4D,G-H). This pattern was replicated in duplicate experiments using different crRNP
212 concentrations (Figure 4H). Destabilizing activity was highly significantly concentrated in
213 regions PR1 and PR2. These findings demonstrate that GCLiPP can provide useful hypothesis-
214 generating data for identifying 3'UTR cis-regulatory elements that contribute to post-
215 transcriptional gene regulation.

216

217 Cross-species comparison of GCLiPP reveals patterns of biochemically shared post-
218 transcriptional regulation

219 Next, we sought to compare RBP occupancy in mouse and human T cells. To do so, we
220 performed Clustal Omega sequence alignments of thousands of human 3' UTRs and their
221 corresponding sequences in the mouse genome, and then designed an algorithm to identify
222 correlated peaks of normalized GCLiPP read density along the aligned nucleotides (Figure 5A).
223 Using this approach, we identified 1047 high-stringency biochemically shared GCLiPP peaks
224 derived from 901 3' UTRs (Supplementary table 1). As a class, biochemically shared peaks
225 exhibited significantly higher sequence conservation than the full 3' UTRs in which they reside
226 (Figure 5B). The highly conserved, biochemically shared peak in *USP25* exemplifies this general
227 pattern (Figure 5C, right panel). However, many biochemically shared peaks did not exhibit
228 corresponding increases in local sequence conservation. For example, the *ARRB2* mRNA that
229 encodes β -arrestin, another regulator of T cell migration in response to chemoattractant gradients
230 (Fong et al., 2002), exhibited a common peak of RBP occupancy in Jurkat cells and primary
231 mouse T cells that is roughly equally conserved as the rest of the 3' UTR (Figure 5C, left panel).

232 To examine which RBPs contributed to biochemically shared peaks more than other
233 GCLiPP peaks, we used HOMER motif calling software (Heinz et al., 2010) to identify enriched
234 motifs. Strikingly, of the six linear sequence motifs present in >10% of biochemically shared
235 peaks with $p \leq 10^{-10}$, five resemble well-known regulatory sequences (Figure 5D). The two most
236 common appeared to represent canonical CELF (Timchenko et al., 1996) and PUM (Hafner et
237 al., 2010) binding motifs. Three other identified motifs corresponded to runs of homo-polymers:
238 An A-rich motif that resembled the canonical polyadenylation signal (Proudfoot, 2011); a poly-U
239 containing motif similar to a sequence that has long been known to stabilize mRNAs (Zubiaga et
240 al., 1995) and a poly-C containing motif similar to the C-rich RNAs bound by poly-C binding
241 proteins (Makeyev and Liebhaber, 2002). We used Metascape (Tripathi et al., 2015) to identify

242 categories of biologically related genes enriched among mRNAs that contained biochemically
243 shared GCLiPP peaks (Figure 5E and Figure 5— source data 2). Interestingly, 3 of the 5 most
244 enriched categories were related to RNA regulation (“regulation of mRNA metabolism,” “large
245 Drosha complex,” “RNA splicing”), with the broad category “post-transcriptional regulation of
246 gene expression” also in the top 10. Thus, biochemically shared GCLiPP binding sites are
247 generally more well conserved than their local sequence context, are enriched for well-studied
248 RBP binding motifs, and occur preferentially in genes that encode proteins involved in post-
249 transcriptional gene regulation, suggestive of conserved autoregulatory gene expression
250 networks.

251 We hypothesized that functionally conserved destabilizing cis-regulatory elements could
252 be identified by examining biochemically shared GCLiPP peaks in 3' UTRs of labile transcripts.
253 To prioritize candidates, we computed Pearson correlation coefficients for the normalized
254 GCLiPP profiles of 3' UTRs of genes expressed in both Jurkat cells and primary mouse T cells
255 (Figure 6A, black histogram) and examined transcript instability by RNAseq analysis of primary
256 mouse T cells treated with actinomycin D (Figure 6A, red histogram). The proto-oncogene *PIM3*
257 emerged as an outstanding candidate with both strong interspecies GCLiPP correlation and very
258 high transcript instability. Alignment of the GCLiPP profiles of human and mouse *PIM3*
259 revealed a dominant shared peak of GCLiPP read density (Figure 6B). This peak corresponded to
260 a highly conserved region of the transcript that contains a G-quadruplex, followed by a putative
261 AU-rich element (ARE) and a CELF binding motif (Figure 6C). Another conserved region with
262 a G-quadruplex followed by a putative ARE appeared upstream of the biochemically shared
263 GCLiPP peak. We numbered these conserved regions CR1 and CR2 according to their order in
264 the 3' UTR, and hypothesized that CR2 would exert greater cis-regulatory activity than CR1,

265 given its RBP occupancy in both species and the relative lack of occupancy in CR1. To test this
266 hypothesis, we performed CRISPR dissections of both the human and mouse *PIM3* 3' UTRs
267 (Figure 6— source data 1). These analyses produced largely concordant patterns of post-
268 transcriptional cis-regulatory activity in the human and mouse 3' with the greatest significant
269 destabilizing effect corresponding to the shared region of GCLiPP read intensity covering the
270 CR2 element (Figure 6D-K). Consistent with this portrait of the entire 3' UTR, when we filtered
271 specifically for mutations that completely deleted either CR1 or CR2, we observed significantly
272 greater expression of transcripts derived from cells with CR2 deleted versus CR1 (Figure 6L,M).
273 Thus, *PIM3* is a very unstable transcript with highly concordant RBP occupancy in human and
274 mouse. Functional dissection of the post-transcriptional regulatory landscape of this gene
275 revealed that this biochemical concordance between mouse and human cells is mirrored at a
276 functional level, with the most highly occupied region indicated by GCLiPP read density
277 corresponding to the most destabilizing region of the 3' UTR.

278

279 **Discussion**

280 Interconnected networks of bound RBPs and RNAs form a complex layer of post-
281 transcriptional regulation that affects all biological processes. Understanding these networks
282 remains one of the key challenges in deciphering how the genome encodes diverse cell identities
283 and behaviors. The outcomes of RNA/RBP interactions can be quite varied. RBP occupancy can
284 affect RNA biogenesis, decay, translation, localization, splicing, chemical modification and
285 editing. Developing a roadmap to understand the cis-regulatory elements in each gene will be
286 critical to full elucidation of the post-transcriptional biology of any given transcript. Biochemical
287 procedures like CLIP that utilize RBP-specific immunoprecipitation have facilitated decoding of

288 these networks for individual RBPs. However, the number of validated CLIP antibodies remains
289 much smaller than the number of RBPs which are known to associate with mature RNAs (Baltz
290 et al., 2012; Sundararaman et al., 2016). In addition, the relative occupancy of cis-regulatory
291 elements bound by different proteins cannot be directly compared using different pools of
292 immunoprecipitated material. Here, we adapted previously described methodologies to arrive at
293 a technique, GCLiPP, to provide such a global RBP occupancy roadmap, and applied this
294 technique to interrogate post-transcriptional cis-regulatory activity in human and mouse T cells.

295 Systematic comparison with eCLIP data for 87 individual RBPs (Sundararaman et al.,
296 2016) indicated that GCLiPP roughly represented a weighted average of all potential eCLIP
297 experiments for cytosolic RBPs. Presumably, this includes proteins that are not appreciated as
298 having RNA binding activity, and those for which no specific affinity reagents are currently
299 available. GCLiPP peaks overlapped eCLIP peaks at a frequency much greater than would be
300 expected by chance, and overall GCLiPP read density correlated with eCLIP read density in a
301 manner that corresponded with the relative abundance of a given RBP in purified cellular
302 mRNPs (Baltz et al., 2012). Nevertheless, the eCLIP peaks for some low abundance RBPs were
303 significantly enriched in GCLiPP profiles. The strongest correlations were observed for abundant
304 cytosolic RBPs, and the correspondence between eCLIP and GCLiPP was only apparent for
305 cytosolic, but not non-cytosolic, RBPs. This result was expected. COMPARTMENTS
306 annotations (Binder et al., 2014) indicate that most of the RBPs classified as non-cytosolic are
307 mainly located in the nucleus, and the GCLiPP protocol includes pelleting nuclei after a gentle
308 detergent based cellular lysis, followed by an enrichment for polyadenylated RNA. Both of these
309 steps would be predicted to selectively eliminate nuclear RNPs associated with primary

310 transcripts. Future iterations of GCLiPP could be modified to intentionally enrich for nuclear
311 RBPs to examine the regulatory landscape of mRNA biogenesis.

312 The GCLiPP datasets described here provide a rich resource for the annotation and
313 experimental dissection of cis-regulatory function in mRNAs. GCLiPP detected RBP occupancy
314 at many known cis-regulatory regions, including canonical polyadenylation signals and elements
315 that control mRNA localization, translation and stability, providing a biochemical correlate of
316 functional activity. In addition, we demonstrated that GCLiPP can guide discovery of novel cis-
317 regulatory elements. Dissection of the *CD69* 3'UTR revealed regions of destabilizing activity
318 that correspond to RBP occupied sites detected by GCLiPP. Our findings corroborate a previous
319 study that identified region PR2 as a potential destabilizing region that contained AREs (Santis et
320 al., 1995). We expanded on this work and further identified a new destabilizing region (region
321 PR1) that also exhibits GCLiPP evidence of RBP occupancy. Further assessment of these post-
322 transcriptional cis-regulatory regions may provide novel insights into immune cell biology.
323 CD69 is an important regulator of T cell differentiation (Martín et al., 2010), migration (Shiow et
324 al., 2006) and metabolism (Cibrian et al., 2016). Because of these effects, CD69 is considered a
325 potential target of therapeutic treatments for autoimmune and inflammatory disorders (González-
326 Amaro et al., 2013). Generation of post-transcriptionally modified T cells expressing high levels
327 of CD69 could provide insight into its role in T cell biology and inflammatory disorders.

328 We leveraged the matched datasets from similar cell types expressing many shared
329 transcripts to perform a cross species comparison of the post-transcriptional regulatory
330 landscape. As might be expected, the sequences of 3' UTR regions that appeared as peaks of
331 RBP occupancy in both species were in general more conserved than the full length 3' UTRs in
332 which they occurred. These biochemically shared peaks were enriched in well-known RBP-

333 binding cis-regulatory sequences including PUM motifs, CELF motifs and canonical
334 polyadenylation signals. Surprisingly, though, we also found clear biochemically shared peaks
335 with relatively poor sequence conservation. These regions retain RBP occupancy despite an
336 evident lack of strong selective pressure on their primary sequence, perhaps due to highly
337 degenerate and/or structural determinants of RBP occupancy. RNAs with conserved structure
338 and RBP binding but poorly conserved primary sequence have been reported before, and they are
339 enriched in gene regulatory regions (Seemann et al., 2017; Weinreb et al., 2016). Finally, we
340 noted that transcripts with biochemically shared peaks tended to encode proteins that were
341 themselves involved in post-transcriptional gene regulation. This pattern is consistent with
342 previous suggestions that auto-regulatory or multi-component feedback loops may be a
343 conserved mode of post-transcriptional gene regulation (Kanitz and Gerber, 2010).

344 Our dissection of the human *PIM3* and mouse *Pim3* 3'UTRs demonstrates the utility of
345 GCLiPP for decoding biochemically shared and functionally conserved post-transcriptional
346 regulation. The PIM family of serine/threonine kinases exert profound regulatory effects on
347 MYC activity, cap-dependent translation independent of MTOR, and BAD mediated antagonism
348 of apoptosis (Narlik-Grassow et al., 2014). Post-transcriptional regulation of PIM kinases is
349 important, as proviral integrations in the *Pim1* 3' UTR are highly oncogenic (Nawijn et al.,
350 2011). *Pim3* mRNA was abundant but highly labile in T cells, with a turnover rate in the top 2%
351 of expressed mRNAs. PIM family members contain multiple ARE like repeats of AUUU(A), but
352 the specific sequences responsible for rapid mRNA decay have not been described and cannot be
353 predicted from the primary sequence alone. The *PIM3* 3'UTR contains two phylogenetically
354 conserved regions with very similar predicted ARE sequences. Of these regions, we predicted
355 that greater regulatory activity would be exerted by the region with GCLiPP evidence for RBP

356 occupancy in both human and mouse cells. CRISPR dissection bore out this prediction in both
357 species. The inactive conserved region may be structurally inaccessible to RBP occupancy, or it
358 may be occupied and exert regulatory activity only in other cell types or signaling conditions.
359 These possibilities further highlight the utility of unbiased biochemical determination of RBP
360 occupancy for annotating the regulatory transcriptome. The datasets reported here will accelerate
361 the annotation of cis-regulatory elements operant in T cell transcripts. In general, GCLiPP can be
362 combined with other unbiased biochemical assays and genetic analyses to yield a roadmap for
363 the dissection of post-transcriptional regulatory networks.

364

365

366 **Materials and Methods**

367 Cells

368 Jurkat cells were grown in RPMI supplemented with fetal bovine serum (Omega). Primary CD4⁺
369 and CD8⁺ mouse T cells were isolated from C57BL/6J mouse peripheral lymph nodes and spleen
370 using positive and negative selection Dynabeads, respectively, according to the manufacturer's
371 instructions (Invitrogen). All mice were housed and bred in specific pathogen-free conditions in
372 the Animal Barrier Facility at the University of California, San Francisco. Animal experiments
373 were approved by the Institutional Animal Care and Use Committee of the University of
374 California, San Francisco. Cells were stimulated with immobilized biotinylated anti-CD3 (clone
375 2C11, 0.25 µg/mL, BioXcell) and anti-CD28 (clone 37.51, 1 µg/mL, BioXcell) bound to
376 Corning 10 cm cell culture dishes coated with Neutravidin (Thermo) at 10 µg/mL in PBS for 3 h
377 at 37 °C. Cells were left on stimulation for 3 days before being transferred to non-coated dishes
378 in T cell medium (Steiner et al., 2011) supplemented with recombinant human IL-2 (20 U/mL).

379 Th2 cell cultures were also supplemented with murine IL-4 (100 U/mL) and anti-mouse IFN- γ
380 (10 μ g/mL). CD8 T cell cultures were also supplemented with 10 ng/mL recombinant murine IL-
381 12 (10 ng/mL). For re-stimulation, cells were treated with 20 nM phorbol 12-myristate 13-
382 acetate (PMA) and 1 μ M ionomycin (Sigma) for 4 hours before harvest.

383

384 Measurement of mRNA Decay

385 Cells were stimulated with PMA and Ionomycin for 4 hours and then additionally treated with
386 Actinomycin-D (Sigma-Aldrich) at 5 μ g/mL for an additional 0, 1, 2 or 4 hours. After treatment,
387 cells were lysed with Trizol LS (Life Technologies) and processed with Direct-zol TM 96 well
388 RNA (Zymogen). RNA was quantified with an ND-1000 spectrophotometer (NanoDrop) and
389 reverse transcribed with SuperScript III First Strand Synthesis Kit (Invitrogen). Quantitative
390 PCR was performed in two separate experiments using SYBR Advantage qPCR Premix
391 (Clontech) on a Realplex 2S instrument (Eppendorf).

392

393 GCLiPP and RNAseq

394 ~100 \times 10⁶ mouse T cells cultured from 3 mice or ~100 \times 10⁶ Jurkat T cells were washed
395 and resuspended in ice cold PBS and UV irradiated with a 254 nanometer UV crosslinker
396 (Stratagene) in three doses of 4000 mJ, 2000 mJ and 2000 mJ, swirling on ice between doses.
397 Cells were pelleted and frozen at -80 °C. Thawed pellets were rapidly resuspended in 400 μ L
398 PXL buffer without SDS (1X PBS with 0.5% deoxycholate, 0.5% NP-40, Protease inhibitor
399 cocktail) supplemented with 2000 U RNasin (Promega) and 10 U DNase (Invitrogen). Pellets
400 were incubated at 37 °C with shaking for 10 min, before pelleting of nuclei and cell debris
401 (17000 g for 5 min). Supernatants were biotinylated by mixing at room temperature for 30 min

402 with 500 μ L of 10 mM EZ-Link NHS-SS-Biotin (Thermo) and 100 μ L of 1 M sodium
403 bicarbonate. Supernatants were mixed with 1 mg of washed oligo-dT beads (New England
404 Biolabs) at room temperature for 30 min and washed 3 times with magnetic separation. Oligo-dT
405 selected RNA was eluted from beads by heating in poly-A elution buffer (NEB) at 65 °C with
406 vigorous shaking for 10 min. An aliquot of eluted RNA was treated with proteinase K and saved
407 for RNAseq analysis using Illumina TruSeq Stranded Total RNA Library Prep Kit according to
408 the manufacturer's instructions. Cells treated with Actinomycin-D as described above were also
409 collected for RNAseq to generate transcriptome wide measurements of transcript stability.

410 The remaining crosslinked, biotinylated mRNA-RBP complexes were captured on 250
411 μ L of washed M-280 Streptavidin Dynabeads (Invitrogen) for 30 min at 4 °C with continuous
412 rotation to mix. Beads were washed 3 times with PBS and resuspended in 40 μ L of PBS
413 containing 1000 U of RNase T1 (Thermo) for 1 min at room temperature. RNase activity was
414 stopped by addition of concentrated (10% w/v) SDS to a final concentration of 1% SDS. Beads
415 were washed successively in 1X PXL buffer, 5X PXL buffer and twice in PBS. 24 pmol of 3'
416 radiolabeled RNA linker was ligated to RBP bound RNA fragments by resuspending beads in 20
417 μ L ligation buffer containing 10 U T4 RNA Ligase 1 (New England Biolabs) with 20% PEG
418 8000 at 37 degrees for 3 h. Beads were washed 3X with PBS and free 5' RNA ends were
419 phosphorylated with polynucleotide kinase (New England Biolabs). Beads were washed 3X with
420 PBS and resuspended in ligation buffer containing 10 U T4 RNA Ligase 1, 50 pmol of 5' RNA
421 linker and 20% PEG 8000 and incubated at 15 °C overnight with intermittent mixing. Beads
422 were again washed 3 times in PBS and linker ligated RBP binding fragments were eluted by
423 treatment with proteinase K in 20 μ L PBS with high speed shaking at 55 °C. Beads and
424 supernatant were mixed 1:1 with bromophenol blue formamide RNA gel loading dye (Thermo)

425 and loaded onto a 15% TBE-Urea denaturing polyacrylamide gel (BioRad). Ligated products
426 with insert were visualized by autoradiography and compared to a control ligation (19 and 24 nt
427 markers). Gel slices were crushed and soaked in gel diffusion buffer (0.5 M ammonium acetate;
428 10 mM magnesium acetate; 1 mM EDTA, pH 8.0; 0.1% SDS) at 37 °C for 30 min with high
429 speed shaking, ethanol precipitated and resuspended in 20 µL of RNase free water. Ligated
430 RNAs were reverse transcribed with Superscript III reverse transcriptase (Invitrogen) and
431 amplified with Q5 polymerase (New England Biolabs). PCR was monitored using a real time
432 PCR thermal cycler and amplification was discontinued when it ceased to amplify linearly. PCR
433 products were run on a 10% TBE polyacrylamide gel, size selected for an amplicon with the
434 predicted 20-50 bp insert size to exclude linker dimers, and purified from the gel (Qiagen).
435 Cleaned up library DNA was quantified on an Agilent 2100 Bioanalyzer using the High
436 Sensitivity DNA Kit before being sequenced. All GCLiPP and RNAseq sequencing runs were
437 carried out on an Illumina HiSeq 2500 sequencer.

438

439 GCLiPP and RNAseq bioinformatics analysis pipeline

440 FastQ files were de-multiplexed and trimmed of adapters. Each experiment was
441 performed on three technical replicates per condition (resting and stimulated) per experiment.
442 Cloning replicates and experiments were pooled in subsequent analyses. Jurkat and mouse T cell
443 trimmed sequence reads were aligned to the hg38 human or mm10 mouse genome assembly
444 using bowtie2, respectively. After alignment, PCR amplification artifacts were removed by de-
445 duplication using the 2-nt random sequence at the 5' end of the 3' linker using a custom script
446 that counted only a single read containing a unique linker sequence and start and end position of
447 alignment per sequenced sample. Peaks of GCLiPP read density were called by convolving a

448 normal distribution against a sliding window of the observed read distribution. A 70 nucleotide
449 window was analyzed centered on every nucleotide within the 3' UTR. For each window, the
450 observed distribution of read density was compared to a normal distribution of the same
451 magnitude as the nucleotide in the center of the window. The Pearson's correlation coefficient
452 was computed for each nucleotide and peaks were defined as local maxima of goodness of fit
453 between observed GCLiPP read density and the normal distribution, requiring a read depth above
454 20% of the maximum read depth in the 3' UTR global minimum of 10 reads. RNAseq reads
455 were aligned using STAR Aligner (<https://github.com/alexdobin/STAR>) (Dobin et al., 2013) to
456 align against the mm10 genome, and gene expression data were calculated as fragments per
457 kilobase per million reads. All custom scripts are available as STAR Methods Key Resource.

458

459 Comparison of GCLiPP to individual eCLIP datasets

460 eCLIP data (Sundararaman et al., 2016) were downloaded via the ENCODE data portal
461 (<http://www.encodeproject.org/>). The first replicate set of bigwig files were downloaded for each
462 RBP deposited online at the time of analysis (December 2017) as well as CLIPper called peaks
463 for the same. To facilitate comparisons with GCLiPP we called GCLiPP peaks in the Jurkat data
464 using CLIPper (Lovci et al., 2013) after re-aligning Jurkat GCLiPP reads to hg19. Correlation
465 analysis was performed with a custom perl script that calculated the Spearman correlation for
466 read depth at each nucleotide in the 3' UTR of all genes that were expressed in each dataset (as
467 determined by CLIP read depth). ~5000-15000 expressed genes were included in the correlation
468 analysis for each RBP. For comparison to mRNP abundancy, log₁₀ RBP mass spectrometry
469 spectra counts were utilized from (Baltz et al., 2012). To stratify RBPs by subcellular
470 localization, data were taken from the COMPARTMENTS database, with RBPs with a

471 localization score of 5 in the cytosol counted as cytosolic and lower counted as non-cytosolic
472 (Binder et al., 2014). All custom scripts are available as STAR Methods Key Resource.

473

474 CRISPR editing

475 Guide RNA sequences were selected using the Benchling online CRISPR design tool
476 (<https://benchling.com/crispr>) with guides selected to target genomic regions of GCLiPP read
477 density. Synthetic crRNAs and tracrRNA (Dharmacon) were resuspended in water at 160 μ M at
478 1:1 ratio and allowed to hybridize at 37 c for 30 m. For CRISPR dissection experiments, all
479 crRNAs were mixed at an equimolar ratio before annealing to tracrRNA. This annealed gRNA
480 complex (80 μ M) was then mixed 1:1 by volume with 40 μ M *S. pyogenes* Cas9-NLS (University
481 of California Berkeley QB3 Macrolab) to a final concentration of 20 μ M Cas9 ribonucleotide
482 complex (RNP). This complexed gRNA:Cas9 RNP was mixed with a carrier solution of salmon
483 sperm DNA (Invitrogen) and diluted to a final concentration between 5-20 μ M. The diluted
484 gRNA:Cas9 RNPs were nucleofected into primary mouse T cells (24 hours after stimulation)
485 with the P3 Primary Cell 96-well Nucleofector™ Kit and into Jurkat cells with the SE Cell Line
486 96-well Nucleofector™ Kit using a 4-D Nucleofector following the manufacturer's
487 recommendations (Lonza). Cells were pipetted into pre-warmed media and then returned to
488 CD3/CD28 stimulation for another two days and expanded an additional 3 days (mouse primary
489 T cells) or cultured for 7-10 days (Jurkat).

490

491

492 Quantification of CD69 protein and mRNA

493 Jurkat cells were gene edited using the CRISPR-Cas9 system as described above. After 3
494 days in culture, cells were washed and stained with anti-human CD69 PE (BioLegend, clone
495 FN50). Samples were acquired on a FACSAria II (BD Biosciences) with CD69^{hi} cells single cell
496 sorted into a 96 well plate and incubated at 37°C at 5% CO₂ to allow generation of single cell
497 clones. To verify editing, gDNA was extracted from Jurkat clones using QuickExtract™ DNA
498 Solution (Epicentre) according to the manufacturer's instructions. Samples were then amplified
499 by PCR using Q5® High Fidelity DNA Polymerase (New England Biolabs). Quantitative PCR
500 reactions were performed on an Eppendorf Realplex 2S thermocycler with the following
501 program: (95°C 60 s; 35 cycles of 95°C 30 s, 58°C 30 s, 72°C 60 s).

502

503 3' UTR dissection

504 3' UTR dissection was performed as described (Zhao et al., 2017). Gene edited cells were
505 harvested into Trizol reagent (Invitrogen) and total RNA was phase separated and purified from
506 the aqueous phase using the Direct-zol RNA miniprep kit with on-column DNase treatment
507 (Zymo). Genomic DNA was extracted from the remaining organic phase by vigorous mixing
508 with back extraction buffer (4 M guanidine thiocyanate, 50 mM sodium citrate, 1 M Tris base).
509 cDNA was prepared with oligo-dT using the SuperScript III reverse transcription kit
510 (Invitrogen). cDNA and genomic DNA were used as a template for PCR using MyTaq 2X Red
511 Mix (Bioline). To equilibrate the number of target molecules and number of PCR cycles between
512 samples, we performed semi-quantitative PCR followed by agarose gel electrophoresis to
513 determine a PCR cycle number where genomic DNA first showed visible bands. This cycle
514 number was then used with a titration of cDNA concentrations and a concentration that amplified
515 equivalently was selected for analysis by deep sequencing. To quantify relative RNA/DNA

516 ratios, cDNA and genomic DNA amplicons were purified using a QIAquick PCR purification up
517 kit (Qiagen) and quantified on an Agilent 2100 Bioanalyzer using the High Sensitivity DNA Kit
518 (Agilent).

519 Amplicons were tagged with the Nextera XT kit (Illumina) and sequenced on an
520 Illumina 2500 HiSeq. Reads were aligned to a custom genome consisting of the targeted PCR
521 amplicon using STAR aligner and mutations were scored using an awk script
522 (<https://github.com/alexdobin/STAR/blob/master/extras/scripts/sjFromSAMcollapseUandM.awk>
523). RNA/DNA read ratios were calculated for all mutations over 20 nucleotides long and less than
524 250 nucleotides long, and relative expression was quantified as the median normalized
525 RNA/DNA ratio for this subset of mutations. Mutations had to have at least 10 reads in both the
526 RNA and gDNA amplicons and mutations with an RNA/DNA ratio of greater than 10 were
527 excluded as outliers. Effect sizes for each nucleotide of the amplicon in each experiment were
528 computed by comparing this median normalized RNA/DNA ratio for all mutations spanning a
529 given nucleotide to all other mutations. Combined p-values were calculated using a Welch's two
530 sample t-test comparing all mutations spanning a given nucleotide with all other mutations.

531

532 Shared peak calling, motif analysis and icSHAPE and Phylogenetic analyses

533 3' UTR alignments of mouse and human were performed by downloading hg38 RefSeq
534 3' UTRs from UCSC genome browser, (<http://genome.ucsc.edu>), identifying syntenic regions of
535 the mouse genome in mm10 with the KentUtils liftOver program
536 (<https://github.com/ucscGenomeBrowser/kent>) and aligning UTRs with Clustal Omega
537 (<http://www.ebi.ac.uk/Tools/msa/clustalo/>) (Sievers et al., 2011). Biochemically shared peaks
538 were called by the following algorithm: Measure normalized GCLiPP read density (i.e. the

539 fraction of the maximal read depth within that 3' UTR) at each position. Calculate correlation
540 between mouse and human normalized signal, as well as observed data and a normal distribution
541 centered at the point being examined in both the mouse and human data tracks. These three
542 Spearman correlations were added together to calculate a numerical score, and shared peaks were
543 defined as local maxima of these scores. To identify high stringency peaks, peaks were only
544 accepted if they 1) had a correlation of >0.75 between mouse and human, 2) had a peak that had
545 a read density of >0.5 of the maximum read density within that 3' UTR in one data track (mouse
546 or human) and >0.2 in the other and 3) had >10 reads at that location in both mouse and human
547 datasets. Biological enrichment of genes with shared peaks was calculated using the Metascape
548 (Tripathi et al., 2015) online interface (<http://metascape.org>) using the default settings, with the
549 exception that a background set of genes was included in the analysis, specifically all genes that
550 contain a called GCLiPP peak in both human and mouse datasets that do not contain a
551 biochemically shared peak.

552 For motif calling, HOMER (Heinz et al., 2010) was used in RNA mode with the
553 “noweight” option to turn off GC correction to search for motifs of width 5, 6 or 7 nucleotides,
554 with otherwise default parameters. The positive sequence set was the mouse and human
555 sequences of the biochemically shared GCLiPP peaks, the negative sequence set was all other
556 GCLiPP called peaks from Jurkat and mouse T cells that were not shared across species. For
557 icSHAPE we used a published bigwig file of locally normalized icSHAPE signal intensity
558 generated in mouse ES cell (Spitale et al., 2015). Conservation of loci in the mouse and human
559 genomes were obtained from the UCSC genome browser as a bigwig of PhyloP scores of
560 conservation across 60 placental mammals (mouse) and 100 vertebrates (human)

561 (<http://hgdownload.cse.ucsc.edu/goldenpath/mm10/phyloP60way/>,

562 <http://hgdownload.cse.ucsc.edu/goldenpath/hg38/phyloP100way/>).

563

564 Oligonucleotide and primer sequences

565 GCLiPP 3' RNA linker: 5'-NNGUGUCUUUACACAGCUACGGCGUCG-3'

566 GCLiPP 5' RNA linker: 5'-CGACCAGCAUCGACUCAGAAG-3'

567 GCLiPP Reverse transcription primer: 5'-

568 CAAGCAGAAGACGGCATAACGAGATNNNNNNCGCTAGTGACTGGAGTTCAGACGTGT

569 GCTCTTCCGATCCGACGCCGTAGCTGTGTAAA-3' (NNNNNN is barcode for

570 demultiplexing)

571 GCLiPP 3' PCR primer: 5'-CAAGCAGAAGACGGCATAACGAGAT-3'

572 GCLiPP 5' PCR primer: 5'-

573 AATGATACGGCGACCACCGAGATCTACACTGGTACTCCGACCAGCATCGACTCAGA

574 AG-3'

575 Read1seq sequencing primer for GCLiPP: 5'-

576 ACACTGGTACTCCGACCAGCATCGACTCAGAAG-3' Index sequencer primer for GCLiPP:

577 5'-GATCGGAAGAGCACACGTCTGAACTCCAGTCAC-3'

578 CD69 gRNA1: CTCAAGGAAATCTGTGTCAG

579 CD69 gRNA2: TCATTCTTGGGCATGGTTAT

580 CD69 gRNA3: CCTGTGATGCTTCTAGCTCA

581 CD69 gRNA4: AATAATGAAATAACTAGGCG

582 CD69 gRNA5: TAATTGAATCCCTTAAACTC

583 CD69 gRNA6: TGATGTGGCAAATCTCTATT

584 PIM3 (human) gRNA1: TGTGCAGGCATCGCAGATGG
585 PIM3 (human) gRNA2: GACTTTGTACAGTCTGCTTG
586 PIM3 (human) gRNA3: GTGGCTAACTTAAGGGGAGT
587 PIM3 (human) gRNA4: AAACAATAAATAGCCCCGGT
588 PIM3 (human) gRNA5: TTGAGAAAACCAAGTCCCGC
589 PIM3 (human) gRNA6: CAGGAGGAGACGGCCCACGC
590 PIM3 (human) gRNA7: TTTATGGTGTGACCCCCTGG
591 PIM3 (human) gRNA8: CCAAGCCCCAGGGGACAGTG
592 Pim3 (mouse) gRNA1: GTTCAATTCTGGGAGAGCGC
593 Pim3 (mouse) gRNA2 CTGGTTCAAGTATCCACCCA
594 Pim3 (mouse) gRNA3: CCATAAATAAGAGACCGTGG
595 Pim3 (mouse) gRNA4: GCTTCCTCCCGCAAACACGG
596 Pim3 (mouse) gRNA5: CTGGTGTGACTAAGCATCAG
597 Pim3 (mouse) gRNA6: TGGAGAAGGTGGTTGCTTGG
598 Primers
599 CD69 F: TGGAATGTGAGAAGAATTTATACTGG
600 CD69 R: GTAATAGAATTGATTTAGGAAAG
601 PIM3 F (human): TCCAGCAGCGAGAGCTTGTGAGGAG
602 PIM3 R(human): TGATCTCCAGACATCTCACTTTTGAAGT
603 PIM3 R2(human):
604 TGAGATAGGTGCCTCACTGATTAAGCATTGGTGATCTCCAGACATCTCACTTTTGA
605 CTG
606 Pim3 F (mouse): GCGTTCAGAGAACTGTGACCTTCG

607 Pim3 R (mouse): TATGATCTTCAGACATTTTCACACTTTTG

608

609 **References**

- 610 Baltz, A.G., Munschauer, M., Schwanhäusser, B., Vasile, A., Murakawa, Y., Schueler, M.,
611 Youngs, N., Penfold-Brown, D., Drew, K., Milek, M., et al. (2012). The mRNA-Bound
612 Proteome and Its Global Occupancy Profile on Protein-Coding Transcripts. *Mol. Cell* *46*, 674–
613 690.
- 614 Bassell, G.J., and Kelic, S. (2004). Binding proteins for mRNA localization and local translation,
615 and their dysfunction in genetic neurological disease. *Curr. Opin. Neurobiol.* *14*, 574–581.
- 616 Beelman, C.A., and Parker, R. (1995). Degradation of mRNA in eukaryotes. *Cell* *81*, 179–183.
- 617 Berry, M.J., Banu, L., Harney, J.W., and Larsen, P.R. (1993). Functional characterization of the
618 eukaryotic SECIS elements which direct selenocysteine insertion at UGA codons. *EMBO J.* *12*,
619 3315–3322.
- 620 Binder, J.X., Pletscher-Frankild, S., Tsafou, K., Stolte, C., O’Donoghue, S.I., Schneider, R., and
621 Jensen, L.J. (2014). COMPARTMENTS: unification and visualization of protein subcellular
622 localization evidence. *Database* *2014*.
- 623 Buenrostro, J.D., Giresi, P.G., Zaba, L.C., Chang, H.Y., and Greenleaf, W.J. (2013).
624 Transposition of native chromatin for fast and sensitive epigenomic profiling of open chromatin,
625 DNA-binding proteins and nucleosome position. *Nat. Methods* *10*, 1213–1218.
- 626 Castello, A., Fischer, B., Eichelbaum, K., Horos, R., Beckmann, B.M., Strein, C., Davey, N.E.,
627 Humphreys, D.T., Preiss, T., Steinmetz, L.M., et al. (2012). Insights into RNA Biology from an
628 Atlas of Mammalian mRNA-Binding Proteins. *Cell* *149*, 1393–1406.
- 629 Chao, J.A., Patskovsky, Y., Patel, V., Levy, M., Almo, S.C., and Singer, R.H. (2010). ZBP1
630 recognition of β -actin zipcode induces RNA looping. *Genes Dev.* *24*, 148–158.
- 631 Cibrián, D., and Sánchez-Madrid, F. (2017). CD69: from activation marker to metabolic
632 gatekeeper. *Eur. J. Immunol.* *47*, 946–953.
- 633 Cibrian, D., Saiz, M.L., de la Fuente, H., Sánchez-Díaz, R., Moreno-Gonzalo, O., Jorge, I.,
634 Ferrarini, A., Vázquez, J., Punzón, C., Fresno, M., et al. (2016). CD69 controls the uptake of L-
635 tryptophan through LAT1-CD98 and AhR-dependent secretion of IL-22 in psoriasis. *Nat.*
636 *Immunol.* *17*, 985–996.
- 637 Corces, M.R., Buenrostro, J.D., Wu, B., Greenside, P.G., Chan, S.M., Koenig, J.L., Snyder,
638 M.P., Pritchard, J.K., Kundaje, A., Greenleaf, W.J., et al. (2016). Lineage-specific and single-cell
639 chromatin accessibility charts human hematopoiesis and leukemia evolution. *Nat. Genet.* *48*,
640 1193–1203.

- 641 Dobin, A., Davis, C.A., Schlesinger, F., Drenkow, J., Zaleski, C., Jha, S., Batut, P., Chaisson,
642 M., and Gingeras, T.R. (2013). STAR: ultrafast universal RNA-seq aligner. *Bioinforma. Oxf.*
643 *Engl.* *29*, 15–21.
- 644 Fong, A.M., Premont, R.T., Richardson, R.M., Yu, Y.-R.A., Lefkowitz, R.J., and Patel, D.D.
645 (2002). Defective lymphocyte chemotaxis in beta-arrestin2- and GRK6-deficient mice. *Proc.*
646 *Natl. Acad. Sci. U. S. A.* *99*, 7478–7483.
- 647 Freeberg, M.A., Han, T., Moresco, J.J., Kong, A., Yang, Y.-C., Lu, Z.J., Yates, J.R., and Kim,
648 J.K. (2013). Pervasive and dynamic protein binding sites of the mRNA transcriptome in
649 *Saccharomyces cerevisiae*. *Genome Biol.* *14*, R13.
- 650 González-Amaro, R., Cortés, J.R., Sánchez-Madrid, F., and Martín, P. (2013). Is CD69 an
651 effective brake to control inflammatory diseases? *Trends Mol. Med.* *19*, 625–632.
- 652 Hafner, M., Landthaler, M., Burger, L., Khorshid, M., Hausser, J., Berninger, P., Rothballer, A.,
653 Ascano, M., Jungkamp, A.-C., Munschauer, M., et al. (2010). Transcriptome-wide identification
654 of RNA-binding protein and microRNA target sites by PAR-CLIP. *Cell* *141*, 129–141.
- 655 Heinz, S., Benner, C., Spann, N., Bertolino, E., Lin, Y.C., Laslo, P., Cheng, J.X., Murre, C.,
656 Singh, H., and Glass, C.K. (2010). Simple combinations of lineage-determining transcription
657 factors prime cis-regulatory elements required for macrophage and B cell identities. *Mol. Cell*
658 *38*, 576–589.
- 659 Johansson, L., Gafvelin, G., and Arnér, E.S.J. (2005). Selenocysteine in proteins-properties and
660 biotechnological use. *Biochim. Biophys. Acta* *1726*, 1–13.
- 661 Kafasla, P., Skliris, A., and Kontoyiannis, D.L. (2014). Post-transcriptional coordination of
662 immunological responses by RNA-binding proteins. *Nat. Immunol.* *15*, 492–502.
- 663 Kanitz, A., and Gerber, A.P. (2010). Circuitry of mRNA regulation. *Wiley Interdiscip. Rev. Syst.*
664 *Biol. Med.* *2*, 245–251.
- 665 Keene, J.D. (2007). RNA regulons: coordination of post-transcriptional events. *Nat. Rev. Genet.*
666 *8*, 533–543.
- 667 Kislaukis, E.H., Zhu, X., and Singer, R.H. (1994). Sequences responsible for intracellular
668 localization of beta-actin messenger RNA also affect cell phenotype. *J. Cell Biol.* *127*, 441–451.
- 669 Lee, F.C.Y., and Ule, J. (2018). Advances in CLIP Technologies for Studies of Protein-RNA
670 Interactions. *Mol. Cell* *69*, 354–369.
- 671 Li, X., Zhou, B., Chen, L., Gou, L.-T., Li, H., and Fu, X.-D. (2017). GRID-seq reveals the global
672 RNA–chromatin interactome. *Nat. Biotechnol.* *35*, 940–950.
- 673 Lovci, M.T., Ghanem, D., Marr, H., Arnold, J., Gee, S., Parra, M., Liang, T.Y., Stark, T.J.,
674 Gehman, L.T., Hoon, S., et al. (2013). Rbfox proteins regulate alternative mRNA splicing
675 through evolutionarily conserved RNA bridges. *Nat. Struct. Mol. Biol.* *20*, 1434–1442.

- 676 Makeyev, A.V., and Liebhaber, S.A. (2002). The poly(C)-binding proteins: A multiplicity of
677 functions and a search for mechanisms. *RNA* 8, 265–278.
- 678 Mariotti, M., Lobanov, A.V., Guigo, R., and Gladyshev, V.N. (2013). SECISearch3 and
679 Seblastian: new tools for prediction of SECIS elements and selenoproteins. *Nucleic Acids Res.*
680 41, e149.
- 681 Martin, K.C., and Ephrussi, A. (2009). mRNA Localization: Gene Expression in the Spatial
682 Dimension. *Cell* 136, 719–730.
- 683 Martín, P., Gómez, M., Lamana, A., Cruz-Adalia, A., Ramírez-Huesca, M., Ursa, M.A., Yáñez-
684 Mo, M., and Sánchez-Madrid, F. (2010). CD69 association with Jak3/Stat5 proteins regulates
685 Th17 cell differentiation. *Mol. Cell. Biol.* 30, 4877–4889.
- 686 Millevoi, S., and Vagner, S. (2009). Molecular mechanisms of eukaryotic pre-mRNA 3' end
687 processing regulation. *Nucleic Acids Res.* gkp1176.
- 688 Narlik-Grassow, M., Blanco-Aparicio, C., and Carnero, A. (2014). The PIM family of
689 serine/threonine kinases in cancer. *Med. Res. Rev.* 34, 136–159.
- 690 Nawijn, M.C., Alendar, A., and Berns, A. (2011). For better or for worse: the role of Pim
691 oncogenes in tumorigenesis. *Nat. Rev. Cancer* 11, 23.
- 692 Papp, L.V., Lu, J., Holmgren, A., and Khanna, K.K. (2007). From Selenium to Selenoproteins:
693 Synthesis, Identity, and Their Role in Human Health. *Antioxid. Redox Signal.* 9, 775–806.
- 694 Proudfoot, N.J. (2011). Ending the message: poly(A) signals then and now. *Genes Dev.* 25,
695 1770–1782.
- 696 Raghavan, A., Ogilvie, R.L., Reilly, C., Abelson, M.L., Raghavan, S., Vasdewani, J., Krathwohl,
697 M., and Bohjanen, P.R. (2002). Genome-wide analysis of mRNA decay in resting and activated
698 primary human T lymphocytes. *Nucleic Acids Res.* 30, 5529–5538.
- 699 Reed, R. (2003). Coupling transcription, splicing and mRNA export. *Curr. Opin. Cell Biol.* 15,
700 326–331.
- 701 Sandberg, R., Neilson, J.R., Sarma, A., Sharp, P.A., and Burge, C.B. (2008). Proliferating cells
702 express mRNAs with shortened 3' untranslated regions and fewer microRNA target sites.
703 *Science* 320, 1643–1647.
- 704 Santis, A.G., López-Cabrera, M., Sánchez-Madrid, F., and Proudfoot, N. (1995). Expression of
705 the early lymphocyte activation antigen CD69, a C-type lectin, is regulated by mRNA
706 degradation associated with AU-rich sequence motifs. *Eur. J. Immunol.* 25, 2142–2146.
- 707 Schwerk, J., and Savan, R. (2015). Translating the Untranslated Region. *J. Immunol.* 195, 2963–
708 2971.

- 709 Seemann, S.E., Mirza, A.H., Hansen, C., Bang-Berthelsen, C.H., Garde, C., Christensen-
710 Dalsgaard, M., Torarinsson, E., Yao, Z., Workman, C.T., Pociot, F., et al. (2017). The
711 identification and functional annotation of RNA structures conserved in vertebrates. *Genome*
712 *Res.* *27*, 1371–1383.
- 713 Shiow, L.R., Rosen, D.B., Brdicková, N., Xu, Y., An, J., Lanier, L.L., Cyster, J.G., and
714 Matloubian, M. (2006). CD69 acts downstream of interferon-alpha/beta to inhibit S1P1 and
715 lymphocyte egress from lymphoid organs. *Nature* *440*, 540–544.
- 716 Sievers, F., Wilm, A., Dineen, D., Gibson, T.J., Karplus, K., Li, W., Lopez, R., McWilliam, H.,
717 Remmert, M., Söding, J., et al. (2011). Fast, scalable generation of high-quality protein multiple
718 sequence alignments using Clustal Omega. *Mol. Syst. Biol.* *7*, 539.
- 719 Spitale, R.C., Flynn, R.A., Zhang, Q.C., Crisalli, P., Lee, B., Jung, J.-W., Kuchelmeister, H.Y.,
720 Batista, P.J., Torre, E.A., Kool, E.T., et al. (2015). Structural imprints in vivo decode RNA
721 regulatory mechanisms. *Nature* *519*, 486–490.
- 722 Steiner, D.F., Thomas, M.F., Hu, J.K., Yang, Z., Babiarz, J.E., Allen, C.D.C., Matloubian, M.,
723 Belloch, R., and Ansel, K.M. (2011). MicroRNA-29 regulates T-box transcription factors and
724 interferon- γ production in helper T cells. *Immunity* *35*, 169–181.
- 725 Sundararaman, B., Zhan, L., Blue, S.M., Stanton, R., Elkins, K., Olson, S., Wei, X.,
726 Van Nostrand, E.L., Pratt, G.A., Huelga, S.C., et al. (2016). Resources for the Comprehensive
727 Discovery of Functional RNA Elements. *Mol. Cell* *61*, 903–913.
- 728 Thurman, R.E., Rynes, E., Humbert, R., Vierstra, J., Maurano, M.T., Haugen, E., Sheffield,
729 N.C., Stergachis, A.B., Wang, H., Vernot, B., et al. (2012). The accessible chromatin landscape
730 of the human genome. *Nature* *489*, 75–82.
- 731 Timchenko, L.T., Miller, J.W., Timchenko, N.A., DeVore, D.R., Datar, K.V., Lin, L., Roberts,
732 R., Caskey, C.T., and Swanson, M.S. (1996). Identification of a (CUG) $_n$ triplet repeat RNA-
733 binding protein and its expression in myotonic dystrophy. *Nucleic Acids Res.* *24*, 4407–4414.
- 734 Tripathi, S., Pohl, M.O., Zhou, Y., Rodriguez-Frandsen, A., Wang, G., Stein, D.A., Moulton,
735 H.M., DeJesus, P., Che, J., Mulder, L.C.F., et al. (2015). Meta- and Orthogonal Integration of
736 Influenza “OMICS” Data Defines a Role for UBR4 in Virus Budding. *Cell Host Microbe* *18*,
737 723–735.
- 738 Tujebajeva, R.M., Copeland, P.R., Xu, X.-M., Carlson, B.A., Harney, J.W., Driscoll, D.M.,
739 Hatfield, D.L., and Berry, M.J. (2000). Decoding apparatus for eukaryotic selenocysteine
740 insertion. *EMBO Rep.* *1*, 158–163.
- 741 Villar, D., Berthelot, C., Aldridge, S., Rayner, T.F., Lukk, M., Pignatelli, M., Park, T.J.,
742 Deaville, R., Erichsen, J.T., Jasinska, A.J., et al. (2015). Enhancer Evolution across 20
743 Mammalian Species. *Cell* *160*, 554–566.
- 744 Weinreb, C., Riesselman, A.J., Ingraham, J.B., Gross, T., Sander, C., and Marks, D.S. (2016).
745 3D RNA and Functional Interactions from Evolutionary Couplings. *Cell* *165*, 963–975.

746 Wilson, M.D., Barbosa-Morais, N.L., Schmidt, D., Conboy, C.M., Vanes, L., Tybulewicz,
747 V.L.J., Fisher, E.M.C., Tavaré, S., and Odom, D.T. (2008). Species-specific transcription in mice
748 carrying human chromosome 21. *Science* 322, 434–438.

749 Zhao, W., Siegel, D., Biton, A., Tonqueze, O.L., Zaitlen, N., Ahituv, N., and Erle, D.J. (2017).
750 CRISPR–Cas9-mediated functional dissection of 3′-UTRs. *Nucleic Acids Res.* 45, 10800–10810.

751 Zubiaga, A.M., Belasco, J.G., and Greenberg, M.E. (1995). The nonamer UUAUUUAUU is the
752 key AU-rich sequence motif that mediates mRNA degradation. *Mol. Cell. Biol.* 15, 2219–2230.

753

754

755

756 **Author Contributions:**

757

758 Author Contributions: A.L. and W.S.Z. performed the experiments and performed bioinformatic

759 analyses. R.K. established the bioinformatic pipeline for small RNA sequencing analysis. W.Z.

760 and D.E. helped design CRISPR dissection experiments. N.Z. consulted on data analysis and

761 interpretation. K.M.A., A.L. and W.S.Z. designed experiments, interpreted the data, and wrote

762 the manuscript. All authors discussed the results and approved the manuscript.

763

764 **Data availability:**

765 Datasets in this paper are available on Gene Expression Omnibus accessions GSE94554 and

766 GSE115886

767

768

769 **Acknowledgements:**

770

771 We thank David Siegel for advice on analyzing pooled crRNP 3′ UTR dissection experiments.

772 A.L. was supported by Cancer Research Institute Irvington Fellowship and the UCSF

773 Immunology T32 training grant T32AI007334. This work was supported by the US National

774 Institutes of Health (HL107202, HL109102, AI128047, HL124285, GM110251), the Sandler

775 Asthma Basic Research Center, and a Scholar Award (K.M.A.) from The Leukemia &
776 Lymphoma Society. The authors declare no conflicts of interest.

777

778

779

780

781

782

783

784

785

786

787

788

789

790

791

792

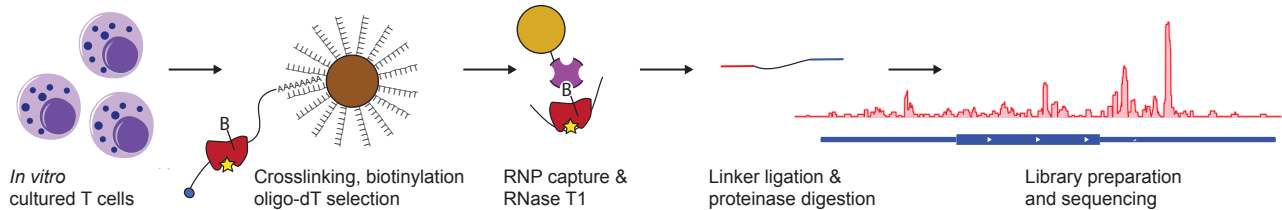
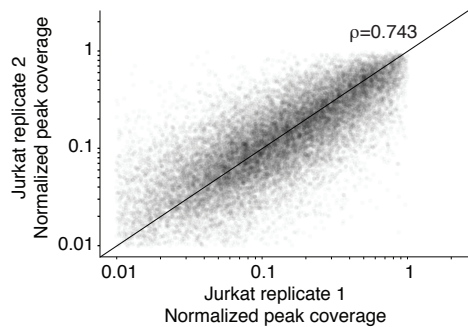
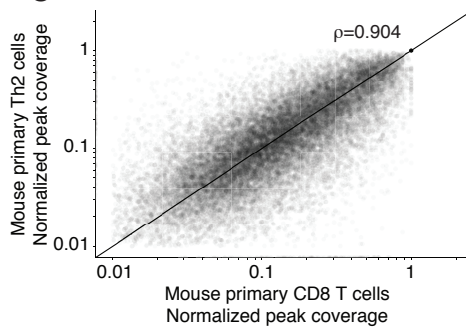
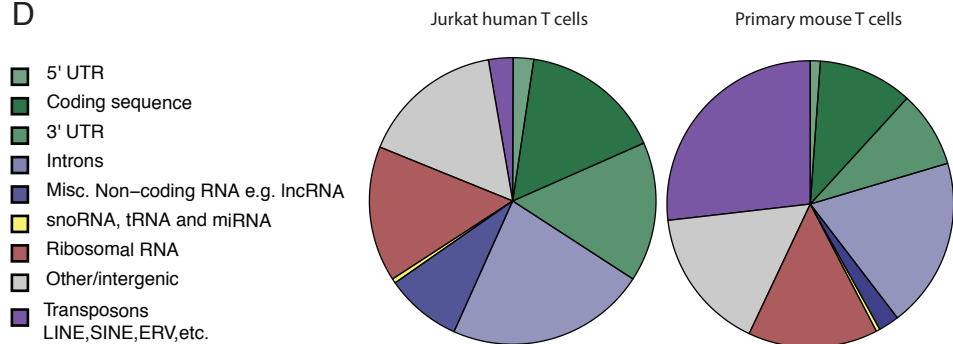
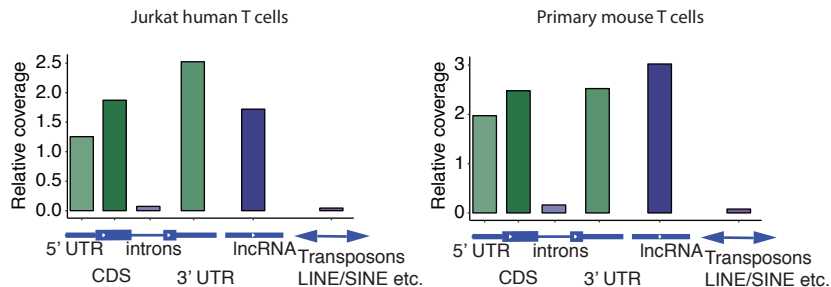
793

794

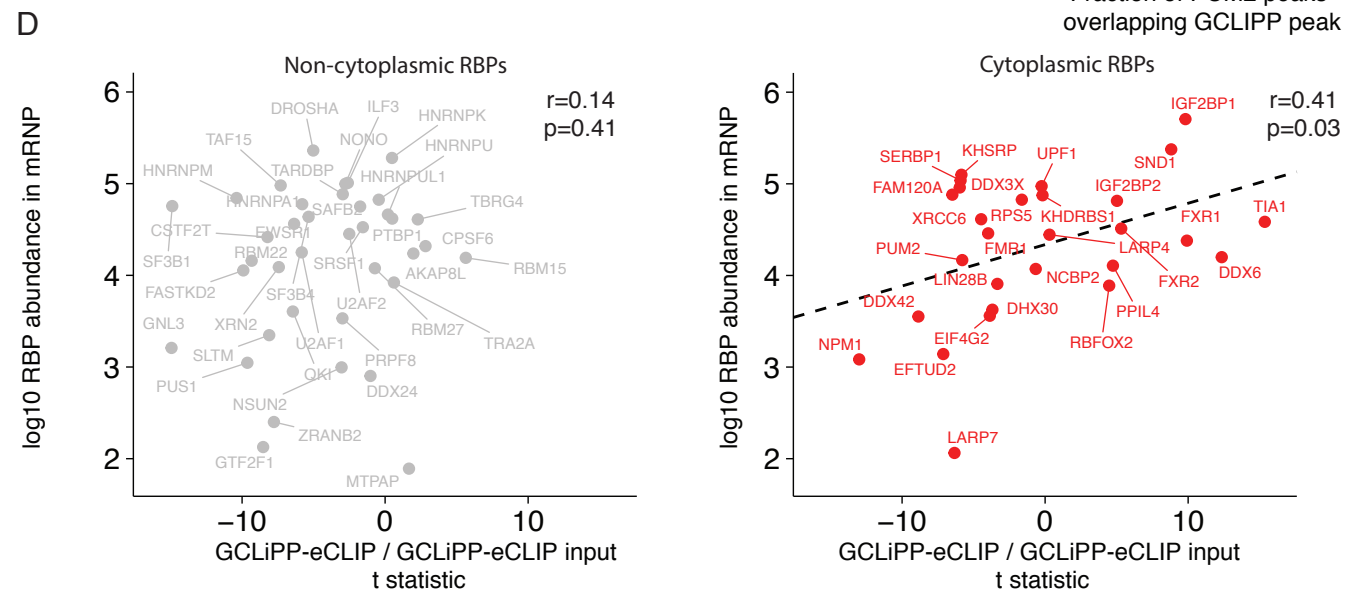
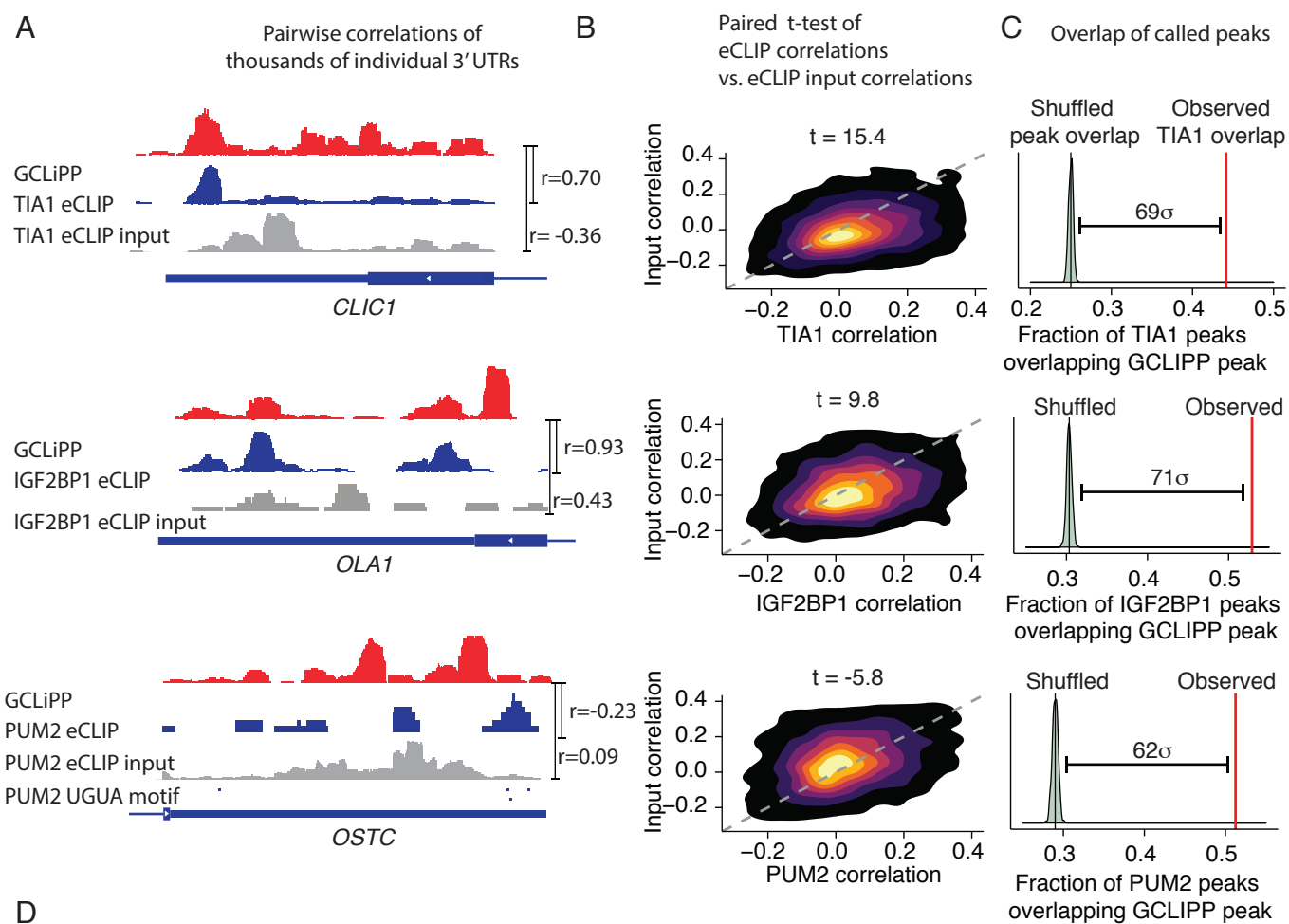
795

796

797

A**B****C****D****E**

798 **Figure 1. GCLiPP sequencing reveals RNA transcript protein occupancy. (A)** GCLiPP
799 method of global RBP profiling. T cell RNAs are crosslinked to RBPs and lysates are
800 biotinylated on primary amines. mRNAs are enriched with oligo-dT beads, and RBP protected
801 sites are digested, captured, sequenced and aligned to the genome. **(B)** Normalized GCLiPP read
802 depth (fraction of reads in called peak relative to all GCLiPP reads in annotated 3' UTR) in two
803 replicates of Jurkat cells. ρ represents Pearson correlation. **(C)** Normalized GCLiPP read depth
804 in mouse primary Th2 and CD8 T cells. ρ represents Pearson correlation. **(D)** Proportion of
805 mapped GCLiPP reads derived from genomic features. **(E)** Relative coverage of genomic
806 features in GCLiPP sequencing reads relative to total length of genomic features of indicated
807 class.
808
809
810
811
812
813
814
815
816
817
818
819



820 **Figure 2. Comparisons with eCLIP reveal abundant cytosolic RBPs drive GCLiPP signal**

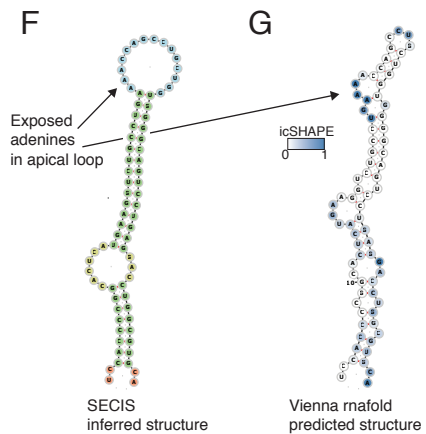
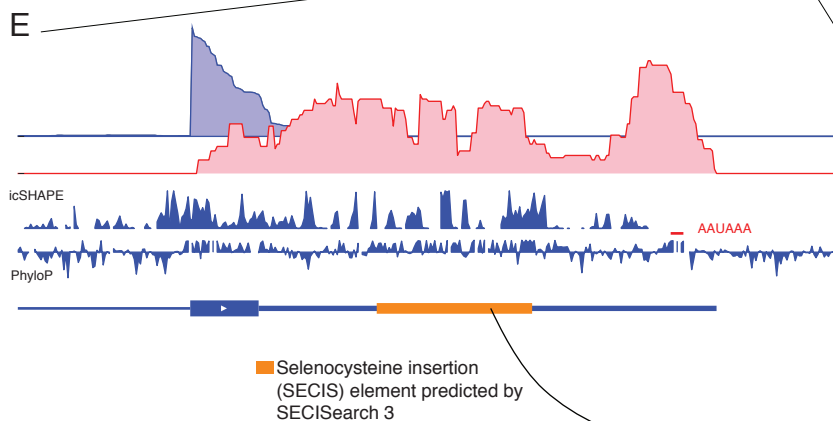
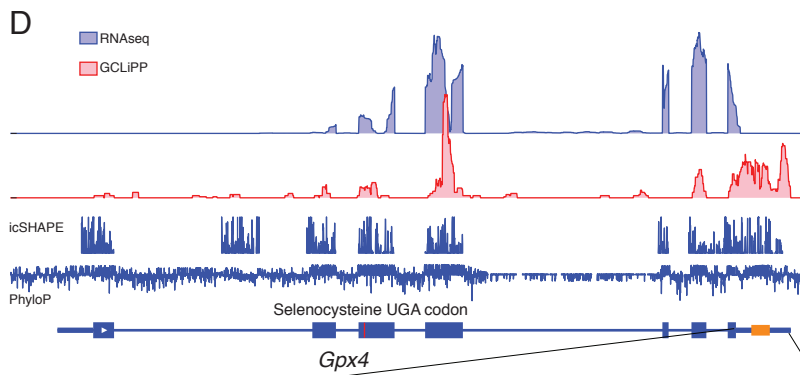
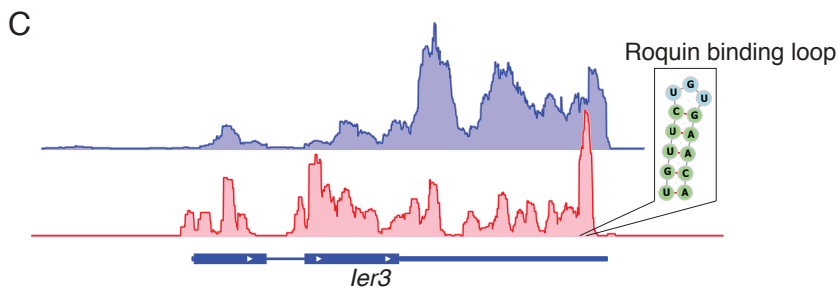
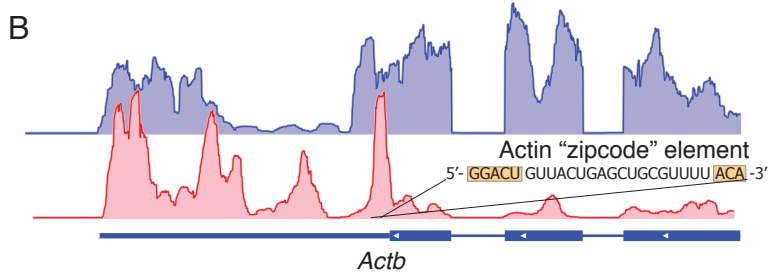
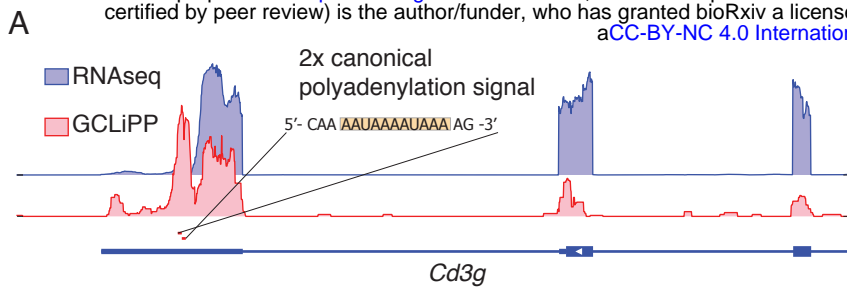
821 (A) Genomic snapshots of individual 3' UTRs showing exemplary correlation between eCLIP
822 datasets and GCLiPP. GCLiPP is shown in red, while the indicated RBP eCLIP data is shown in
823 blue, and matched control input samples are shown in gray, shown for the 3' UTRs of the
824 indicated gene. r indicates Pearson correlation between pairs of normalized read density at a
825 given nucleotide for the indicated comparisons. (B) 2D density plots showing matched
826 correlations between GCLiPP and eCLIP for the indicated RBP (X-axis) and GCLiPP and the
827 matched control input sample (Y-axis) for individual 3' UTR for all expressed genes in eCLIP
828 and GCLiPP datasets. The t -statistic shown is for a paired t -test of the correlations. (C) Overlap
829 of CLIPper called peaks in 3' UTRs in GCLiPP and eCLIP. Red lines indicate observed overlap
830 of GCLiPP peaks and eCLIP peaks. Green distribution represents bootstrapped expected overlap,
831 computed by shuffling called eCLIP peaks within the same 3' UTR, computing overlap of
832 shuffled set with GCLiPP called peaks, and repeating this analysis 500 times. The indicated
833 distance represents the number of standard deviations above the mean shuffled overlap of the
834 observed overlap. (D) Correlation of eCLIP-GCLiPP paired t -tests (from (B) and RBP
835 abundance in mRNPs). RBPs shown in gray score are not cytosolic localized (<5 cytosolic
836 according to COMPARTMENTS) whereas RBPs in red are cytosolic localized (5 cytosolic
837 according to COMPARTMENTS).

838

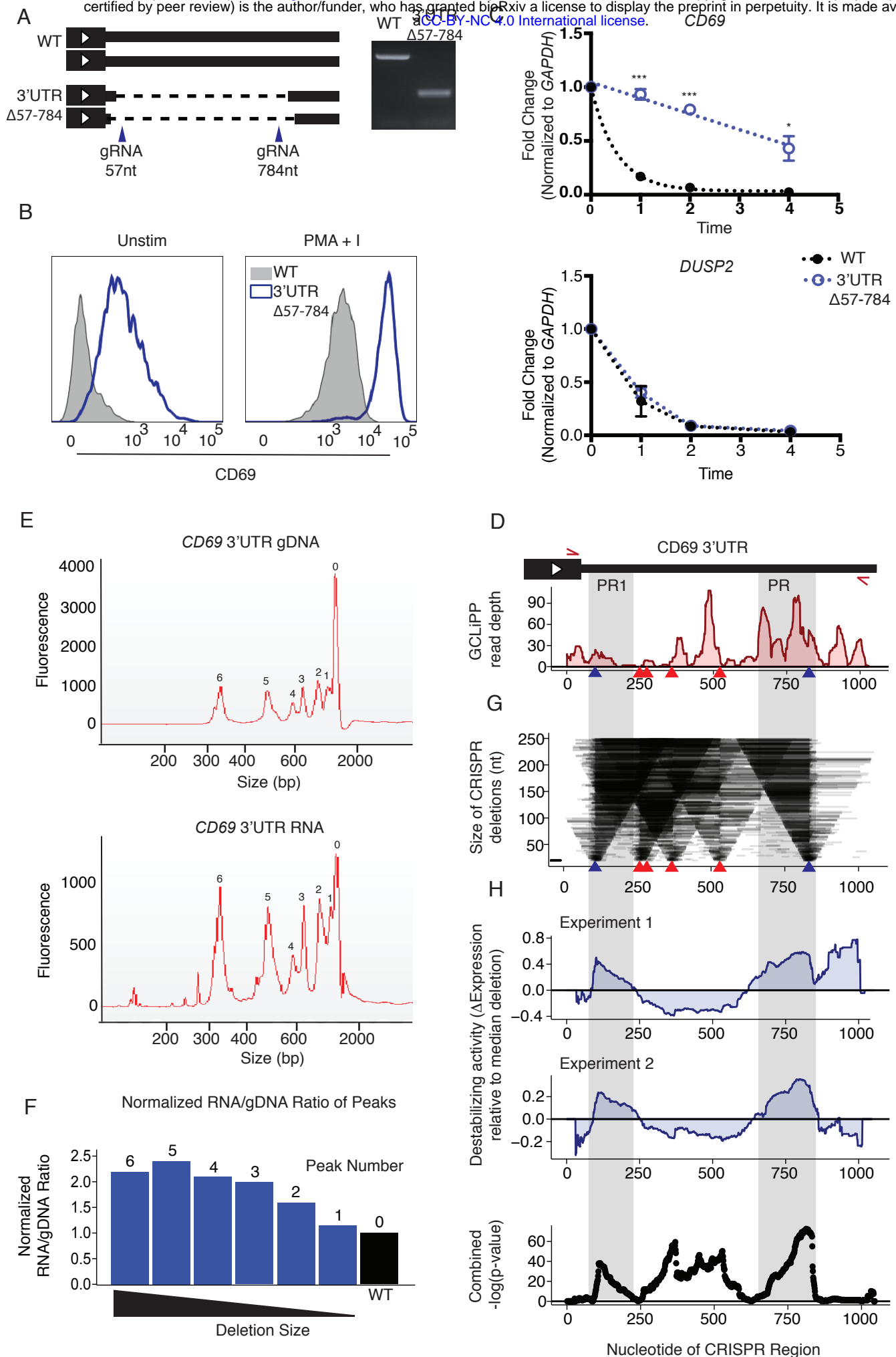
839

840

841



842 **Figure 3. GCLiPP recapitulates previously described mRNA-RBP interactions in primary**
843 **T cells.** RNAseq and GCLiPP tracks for **(A) *Cd3g* (B) *Actb* (C) *Ier3*** and **(D-G) *Gpx4***. RNAseq
844 track is from resting Th2 cells. GCLiPP is sum of five experiments, three in Th2 and two in CD8
845 T cells. Location of known RBP binding determinants are shown as insets.



867 **Figure 4. GCLiPP guides identification of destabilizing regions in CD69 3'UTR. (A)**
868 Schematic illustration and gel image of Jurkat WT and CD69 3'UTR edited clone (3'UTR Δ 57-
869 784). Editing was performed using CRISPR-Cas9 and verified through PCR. Blue arrows
870 indicate gRNA placement with their positions in the 3'UTR indicated by nucleotide (nt) number.
871 (B) CD69 protein expression of WT and 3'UTR Δ 57-784 clone as measured by flow cytometry.
872 Cells were either untreated or stimulated with PMA and Ionomycin (PMA + I) for 4 hours. (C)
873 mRNA decay of *CD69* (top) and *DUSP2* (bottom) transcript in WT and 3'UTR Δ 57-784 clones.
874 Cells were stimulated for 4 h with PMA+I and then treated with Actinomycin-D (act-D).
875 Transcript expression was measured 0, 1, 2 or 4 hours post addition of act-D by qPCR and
876 normalized to *GAPDH* expression. Data was generated from two separate experiments each with
877 N=2 and significance was calculated using multiple t-test corrected with Holm-Sidak method
878 * $p < 0.05$, ** $p < 0.01$, *** $p < 0.001$ (D-H) CRISPR-Cas9 dissection of *CD69* 3'UTR. (D) CD69
879 3'UTR GCLiPP peaks aligned to schematic illustration of 3'UTR. Red arrows indicate primer
880 position during PCR amplification of gDNA and RNA from pooled crRNP transfected Jurkats.
881 Arrow heads represent gRNA placement. Blue arrow heads were gRNAs also used in experiment
882 in Figure 4A. (E) Microfluidic capillary electrophoresis of CD69 3'UTR gDNA (top) and reverse
883 transcribed cDNA (bottom). Individual fragments identified by the Agilent Bioanalyzer software
884 are indicated by the numbers on the graph. (F) Ratio of RNA/gDNA for each labeled peak in (D)
885 normalized to predicted wild-type allele (black bar). Estimated molarity of each peak from the
886 electrophoresis was used to calculate RNA/gDNA ratio. The labeled peaks are plotted in
887 descending order based on deletion size. (G) Size of deletions generated using CRISPR-Cas9.
888 Arrow heads represent gRNA placement as mentioned for Figure 4D. (H) Change in expression
889 along the 3'UTR relative to median expression of all possible deletions. Per-nucleotide effect

890 score was calculated by comparing median normalized RNA/gDNA ratio for all shown deletions
891 spanning a given nucleotide with all shown deletions. Experiment 1 and 2 are duplicate samples
892 which were transfected with 80 μ M or 120 μ M of gRNAs respectively. Grey shaded area PR1 and
893 PR2 indicate regions of significant destabilizing activity. Unadjusted $-\log_{10}$ p-values from
894 Welch's two sample t-test comparing all deletions spanning a nucleotide with all other deletions
895 across both experiments (bottom).

896

897

898

899

900

901

902

903

904

905

906

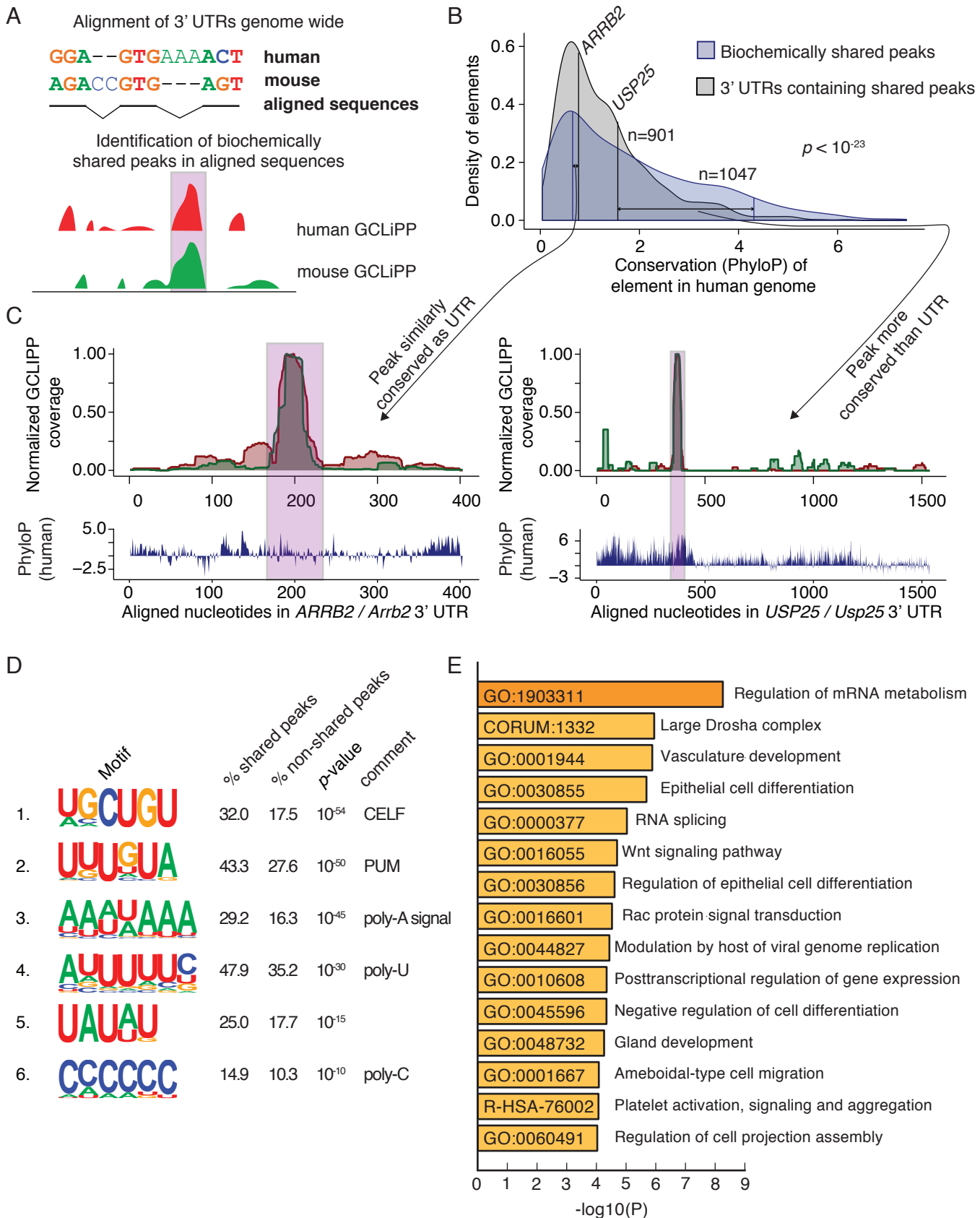
907

908

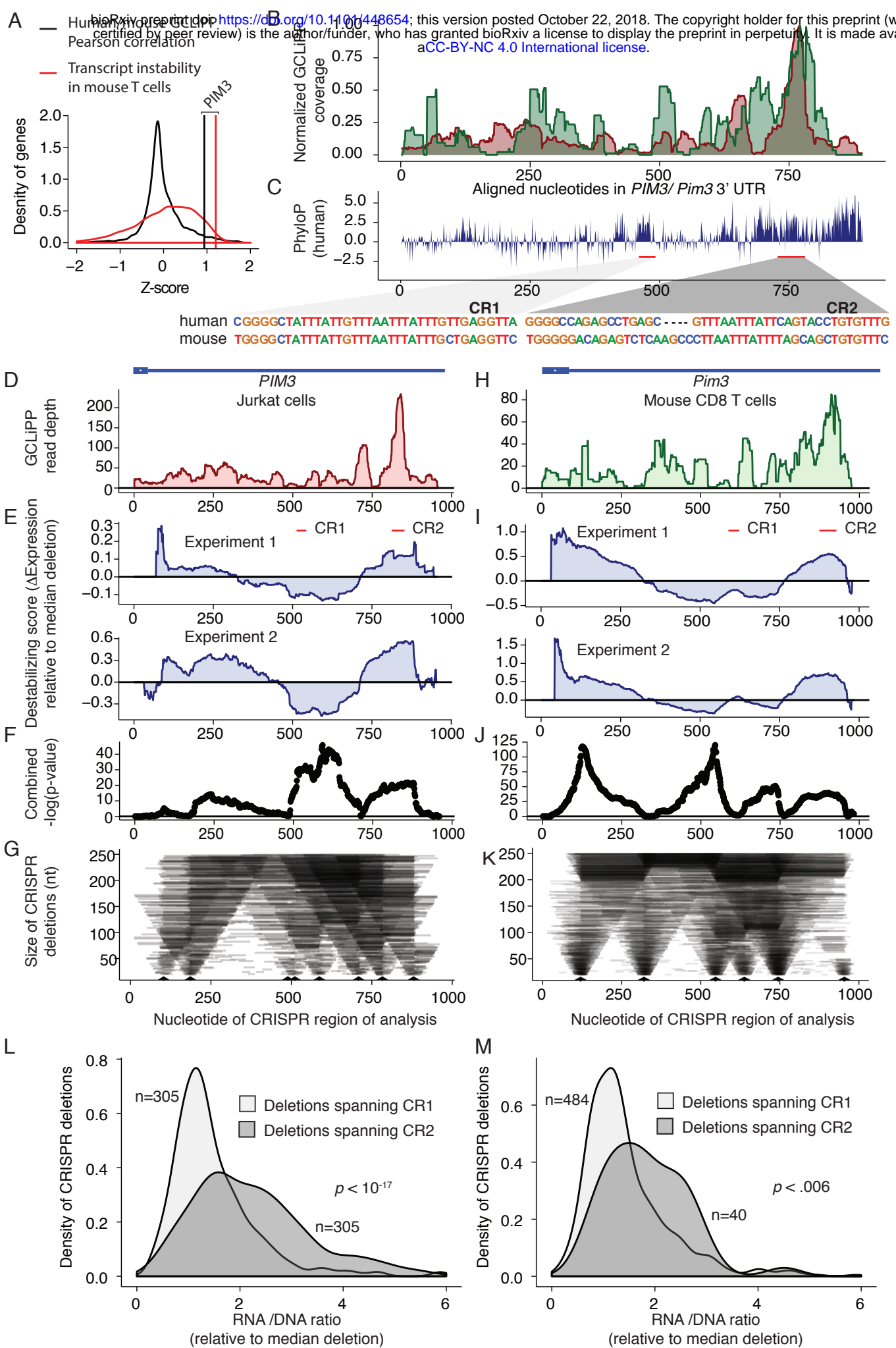
909

910

911



912 **Figure 5. Comparison between mouse and human GCLiPP reveals principles of shared**
913 **post-transcriptional regulation. (A)** Schematic illustration of 3' UTR alignment and
914 biochemically shared GCLiPP peak calling. **(B)** Distribution of conservation across 100
915 vertebrates (PhyloP score) of regions in the human genome. Blue indicates biochemically shared
916 peaks, gray indicates the 3' UTRs of the transcripts that those peaks are contained within. For
917 both peaks within *ARRB2* and *USP25*, their matched conservation of peak and UTR are indicated
918 by connected vertical lines. **(C)** Human and mouse normalized GCLiPP density and conservation
919 (PhyloP) across aligned nucleotides of the indicated 3' UTRs. Biochemically shared peaks of
920 GCLiPP read density are indicated in pink. **(D)** HOMER called motifs enriched in biochemically
921 shared peaks. Percentages indicate the frequency of occurrence of the indicated motif in
922 biochemically shared peaks versus non-shared background peaks. P-value indicates HOMER
923 calculated p-value of enrichment. **(E)** Metascape called biological enrichment categories of
924 genes containing biochemically shared peaks. The background set was all genes that contained
925 peaks in both mouse and human GCLiPP datasets that did not contain a shared peak.
926
927
928
929
930
931
932
933



934 **Figure 6. Biochemically and functionally shared post-transcriptional regulation of PIM3 in**
935 **human and mouse cells. (A)** Z-scores of Pearson correlation between mouse and human
936 GCLiPP (black distribution) and transcript instability as measured by comparing transcript read
937 abundance in untreated versus actinomycin treated mouse T cells (red distribution) for 7541
938 genes with matched data. Vertical lines indicate observations for PIM3. **(B)** Normalized human
939 and mouse GCLiPP read density and **(C)** PhyloP across aligned nucleotides of PIM3 3' UTR (as
940 depicted in Figure 5). Insets show sequences of putative regulatory elements. **(D-L)** Dissection
941 of human PIM3 3'UTR in Jurkat T cells **(D)** GCLiPP peaks aligned to schematic illustration of
942 3'UTR. **(E)** Change in expression along the 3'UTR relative to median expression of all possible
943 deletions. Per-nucleotide effect score was calculated by comparing median normalized
944 RNA/gDNA ratio for all shown deletions spanning a given nucleotide with all shown deletions.
945 Experiment 1 and 2 are biological duplicates which were transfected with 80 μ M or 120 μ M of
946 gRNAs respectively. Red bars indicate putative ARE-containing cis regulatory elements. **(F)**
947 Unadjusted $-\log_{10}$ p-values from Welch's two sample t-test comparing all deletions spanning a
948 nucleotide with all other deletions across both experiments. **(G)** Size of deletions generated using
949 CRISPR-Cas9. Arrow heads represent gRNA placement. **(H-K)** Dissection of mouse PIM3
950 3'UTR. Data are represented identically to human data, except that mouse primary CD8 T cells
951 were used, and both mouse experiments 1 and 2 used a gRNA concentration of 80 μ M. **(L)** Effect
952 of deletions spanning putative ARE containing cis-regulatory elements. The RNA/DNA ratio for
953 mutants deleting ARE1 and ARE2 are shown in human Jurkat T cells. **(M)** Same as in **(L)** but
954 using data from mouse primary T cells.
955